Cellulose Nanocrystal-Templated Tin Dioxide Thin Films for Gas Sensing

Alesja Ivanova[a], Bruno Frka-Petesic[a], Andrej Paul[b], Thorsten Wagner[b], Askhat N. Jumabekov[c], Yury Vilk[d], Johannes Weber[e], Jörn Schmedt auf der Günne[e], Silvia Vignolini[a], Michael Tiemann[b], Dina Fattakhova-Rohlfing[d] and Thomas Bein*[d]

[a]Department of Chemistry, University of Cambridge, Lensfield Road, CB2 1WE, Cambridge, United Kingdom

[b]Department of Chemistry, Faculty of Science, University of Paderborn, Warburger Str. 100, D-33098 Paderborn, Germany

[c]Department of Physics, Nazarbayev University, 53 Kabanbay Batyr Avenue, Nur-Sultan 010000, Kazakhstan

[d]Department of Chemistry and Center for NanoScience (CeNS), University of Munich (LMU), Butenandtstrasse 5-13 (E), 81377 Munich, Germany

[e]Department Chemie und Biologie, Universität Siegen, Adolf-Reichwein-Str. 2, 57076 Siegen, Germany

AUTHOR EMAIL ADDRESS: bein@lmu.de
KEYWORDS: cellulose nanocrystals, biotemplating, porous tin dioxide films, gas sensing
Dedicated to Dr. Klaus Römer at the occasion of his 80th birthday

1. Abstract

Porous tin dioxide is an important low-cost semiconductor applied in electronics, gas sensors and biosensors. Here we present a versatile template-assisted synthesis of nanostructured tin dioxide thin films using cellulose nanocrystals (CNCs). We demonstrate that structural

features of CNC-templated tin dioxide films strongly depend on the precursor composition. The precursor properties were studied by using low-temperature nuclear magnetic resonance spectroscopy of tin tetrachloride in solution. We demonstrate that it is possible to optimize the precursor conditions to obtain homogeneous precursor mixtures and therefore highly porous thin films with pore dimensions in the range of 10 - 20 nm (A_{BET} = 46 - 64 m^2 g^{-1}, measured on powder). Finally, by exploiting the high surface area of the material we developed a resistive gas sensor based on CNC-templated tin dioxide. The sensor shows high sensitivity to carbon monoxide (CO) in ppm concentrations and low cross-sensitivity to humidity. Most importantly, the sensing kinetics is remarkably fast; both the response to the analyte gas and the signal decay after gas exposure occur within few seconds, faster than in standard SnO$_2$-based CO sensors. This is attributed to the high gas accessibility of the very thin porous film.

2. Introduction

Nanoscale tin dioxide is a widespread semiconductor with a broad range of applications, including pigment production, chemical catalysis, exhaust gas treatment and pollution gas sensing.[1-3] The latter applications are based on the ability of tin oxide to favor chemical reactions at the surface and the possibility to create porous thin films with large surface areas. Porosity in such films is generally achieved by combining sol-gel wet-chemical synthesis routes with templates. So far template-assisted wet-chemical techniques have been exploited to design tailorable oxide dimensions and morphologies. Polymers are common structure directors for the synthesis of nanostructured tin dioxide with near-spherical pores and 3D hierarchical structure.[1,4-7] The porous structure is achieved by using evaporation-induced self-assembly (EISA)[8] of polymeríc templates and inorganic precursors followed by template removal. Such nanomaterials are exploited to fabricate porous scaffolds for many devices

including solar cells, gas sensors, biosensors and electrocatalysis. [9-12]

In addition to synthetic polymers, biological materials and biopolymers offer diverse synthesis routes for tailoring the morphology of tin dioxide nanomaterials. For example, tubular structures[13] have been fabricated by coating cotton fibers with tin oxide precursor for Li-ion storage and gas sensing. [14-16] Tin tetrachloride sol-gel chemistry was combined with lyotropic liquid crystals of ethyl–cyanoethyl cellulose.[17] In other work, hydroxypropyl cellulose (HPC) was mixed with tin tetrachloride to obtain tin-doped HPC liquid crystals.[18] Regenerated cellulose was coated with a thin SnO_2 layer via liquid-phase deposition to create flexible hybrid nanocomposites.[19] Furthermore, 3D hierarchical porous structures of tin dioxide were prepared by templating with biological pollen coats and grapefruit exocarp.[20,21] D-glucose monohydrate or cellulose nanofibrils can also be used to assist in the synthesis of tin oxide particles.[22,23]

Cellulose nanocrystals (CNCs) have recently attracted substantial interest as versatile bio-inspired templates for synthesizing functional metal oxides for energy conversion, medicine, sensing and catalysis.[24-33] The porous structures are formed by combining colloidal dispersions of cellulose nanocrystals with metal oxide precursor followed by solvent and template elimination via calcination. To maintain high colloidal stability of CNCs, metal oxide precursors of low reactivity are commonly used, including stabilized pre-formed crystalline nanoparticles or silica precursors with slow hydrolysis-condensation dynamics.[34-37] In contrast to silica precursors, non-silicates exhibit greater sol-gel reactivity and tend to form precipitates in solution leading to limited control of the porosity of the final material.[38-41] Moreover, the overall negative charge of cellulose nanocrystals (CNCs) can be compensated by positively charged polyvalent cations, leading to CNC aggregation.[42]

Here we demonstrate the fabrication of tin oxide thin films by using a facile wet-chemical route based on templating with CNCs. By studying the colloidal properties of CNCs and tin

oxide precursor, we demonstrate different approaches toward tailoring the morphology of tin oxide porous films. The newly developed fabrication procedure is scalable as it uses common chemicals and solvents and it provides reproducible mesoporous films with high crystallinity. Such films can be used as active nanomaterial in diverse applications for catalysis, remediation systems and sensing. To further demonstrate the applicability of cellulose-templated tin dioxide, we developed a resistive gas sensor demonstrating strong and remarkably fast sensor response.

3. Experimental Section

3.1 Synthesis

Extraction of Cellulose Nanocrystals (CNCs)

Cellulose nanocrystals were obtained as reported elsewhere.[43,44] Whatman No. 1 cellulose filter paper (60 g) was hydrolyzed with sulfuric acid (64 wt%, 840 mL) at 60 °C for 30 min, before being quenched with Milli-Q ice and water. Soluble cellulose residues and acid excess were removed by centrifugation (three steps at 20,000 g for 20 min) and dialysed against deionized water (MWCO 12−14 kDa membrane) for 6 days, and a stable viscous suspension of 2.33 wt% CNC was obtained. Conductivity measurements revealed 860 μS/cm conductivity of the final suspension, while conductivity titration against sodium hydroxide indicated $[H^+] = [-OSO_3^-] = 240$ mmol·kg^{-1} on the CNC surface.[45] The suspension was tip-sonicated in an ice bath (Fisherbrand Ultrasonic disintegrator 500 W, amplitude 30% max 9890 J·g^{-1} of CNC) and vacuum-filtered (8.0 μm then 0.8 μm nitrocellulose, Sigma-Aldrich). The as prepared 2.33 wt% suspension was concentrated using a PEG method. The suspension was placed in a dialysis bag (MWCO 12-14 kDa) and covered by 35 kDa PEG (poly(ethylene) glycol, Sigma-Aldrich) until 12.6 wt% CNC concentration was reached.

Tin tetrachloride solutions for the NMR analysis

Table S1 in the Supporting Information (SI) demonstrates the recipes of the tin tetrachloride solutions investigated by using NMR analysis. 0.35 mL tin(IV) chloride (99.9%, Sigma Aldrich) was dissolved under stirring in 4 mL absolute ethanol ("neutral" sample). Then 0.2 mL water, 1 mL concentrated HCl or 0.3 – 0.59 mL 2M aq. NH_4OH were introduced to prepare "neutral+H_2O", "acidic" and "basic" samples, respectively. The addition of base introduced turbidity, hence the measurements were performed after 10 - 30 min stirring at RT, when the solutions became transparent again.

CNC and tin tetrachloride solutions for optical imaging

A CNC stock solution of 12.6 wt% was added to 1.1 M $SnCl_4$ (99.9%, Sigma Aldrich) in water or ethanol. Then water, HCl conc. or 2.0 M NaOH were introduced to reach 0.2 M $SnCl_4$, 2 wt% CNC (SnO_2:CNC=1.5 g/g) and 1.0 M HCl or 0.5 M NaOH concentrations. The solutions were stirred for 1 – 15 h. Afterwards, 5 µL of a solution was cast on a glass slide, dried at room temperature and analyzed by using optical microscopy in dark field mode.

CNC-templated tin oxide thin films

The optimized precursor recipe contained 0.2 M Sn^{4+} and 2 wt% CNC in water (SnO_2:CNC calculated ratio = 1.5 g/g). The solution was prepared by adding 0.453 g of 12.6 wt% CNC to 0.5 mL of 1.1 M aqueous $SnCl_4$ (99.9%, Sigma Aldrich), followed by addition of 1.85 mL water. For the 0.05 M and 0.3 M $SnCl_4$ solutions, the amount of cellulose was fixed at 2 wt% and tin tetrachloride contents were adjusted accordingly. The mixture was stirred for 2 h, afterwards 10 µL was cast on Si-substrate. The as-prepared films were calcined for 1 h at 400 °C. The calcination temperature was reached by applying a heating rate of 2 °C/min.

3.2   Characterization

Transmittance spectra of the $SnCl_4$/CNC solutions were obtained with a Lambda 950 PerkinElmer UV/Vis spectrometer in a 1 mm quartz cuvette.

For the ^{119}Sn static NMR measurements the sample was put into a glass container made from a reshaped commercial 5 mm Duran™ NMR tube (Figure S1 in the SI). The ampule was filled with the solution, immersed in liquid nitrogen for a short time and then sealed by melting glass at its narrow end. The opposite end of the ampule with an increased amount of glass served to correct the center of sample mass during NMR measurements. For the [117]Sn MAS NMR experiments, the solution was placed into a commercial 4 mm Bruker MAS probehead in a plastic tube and closed by gluing a lid on top.

NMR measurements were performed on a Bruker Avance 500 DSX spectrometer equipped with a 11.75 T magnet at temperatures from 190 K to RT. The spectra were recorded on a deshielding scale in the range from −850 to −400 ppm relative to neat tetramethylstannane. Calibration of the spectrometer was performed with the aid of the Ξ parameter with tetramethylsilane.[46]

Optical characterization was performed in reflection mode on a customized Zeiss (Axio Scope.A1 Vario) microscope using a halogen lamp (Zeiss HAL100) as a light source using Koehler illumination. Samples were observed with a 20x Zeiss Epiplan Apochromat objective in bright field (BF) and dark field (DF).

Top views of CNC-templated tin dioxide thin films were analyzed using a JEOL JSM-6500F scanning electron microscope equipped with a field emission gun, at 10 − 20 kV. Transmission electron microscopy was performed using a FEI Titan 80−300 instrument equipped with a field emission gun operated at 300 kV.

X-ray diffraction analysis was carried out in reflection mode by using a Bruker D8 diffractometer with 1.5406 Å Ni-filtered Cu Kα radiation, operating at 40 kV and 40 mA. The mean crystallite size was estimated from the broadening of the (110) cassiterite reflection by using the Scherrer equation.[47]

The nitrogen sorption isotherms were obtained at −196 °C using a Quantachrome Autosorb-1. Before the measurements, ca. 25 mg of the sample was outgassed at 150 °C under vacuum overnight. The specific surface area was determined with the Brunauer−Emmett−Teller (BET) method in the range of $p/p_0 = 0.05−0.2$. The pore size distribution was determined using a slit/cylindrical pore NLDFT equilibrium model by using the Quantachrome Instruments Autosorb-1 software.[48] X-ray di raction and nitrogen sorption analysis was performed on pulverized free-standing films obtained by casting and calcining precursor solutions.

Gas sensing measurements were carried out by using a sensor substrate with interdigitated platinum electrodes on an alumina plate ($3×3$ mm^2; electrode distance 20 μm) with integrated platinum heater (Pt 10) to control the temperature of the sensing layer (UST Umweltsensortechnik GmbH, Germany[49]). Tin dioxide films were prepared directly on the sensor substrates: 1 μL of the aqueous precursor solution (0.2 mol L^{-1} SnCl$_4$ and 2 wt% CNC, corresponding to a SnO$_2$:CNC ratio of 1.5 g/g) was drop-cast onto the plasma-cleaned substrate and subsequently calcined for one hour at 400 °C (2 °C min^{-1} heating rate). The gas atmosphere under flowing conditions was provided by a custom-built, computer-controlled setup based on mass flow controllers (Brooks Instruments). The analyte gas (CO) concentration was varied (from 5 ppm to 90 ppm) by mixing with synthetic air. The relative humidity (r.h.) was varied (30 %, 50%, and 70 %) by mixing dry synthetic air with water vapor-saturated synthetic air (100 % r.h.) at room temperature. The total gas flow was 500 mL min^{-1}. The change in ohmic resistance of the sensing layer (sensor response) was measured by custom-built electronics in potentiostatic mode with a measurement voltage of 0.5 V. The sensing temperature was set by a PID-controller. For comparison, a commercial SnO$_2$-based reference sensor UST GGS 1330 was used.

4. Results and Discussion

To prepare porous CNC-templated films, tin tetrachloride was mixed with the templating species, then the mixture was deposited on a substrate and heated to decompose the template. Figure 1 shows that both the pristine solution of $SnCl_4$ and the aqueous CNC suspension are transparent and clear, while, after mixing, the suspension becomes very turbid, indicating aggregation and/or precipitation of the CNCs.
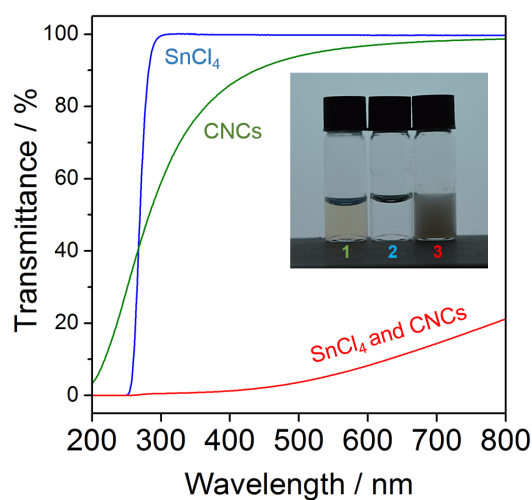

Figure 1. Transmittance spectra of (1) 2 wt% CNC suspension, (2) 0.2 M $SnCl_4$, and (3) mixture of 2 wt% CNC and 0.2 M $SnCl_4$ in water. The inset shows a photograph of the corresponding solutions taken under back light illumination.

The phase separation in a precursor solution can negatively affect the film homogeneity and overall porous film morphology. Therefore, to better control precursor homogeneity, and possibly prevent aggregation, we studied the sol-gel transformation of pristine tin tetrachloride by using solid state NMR spectroscopy.

The transformation of molecular tin tetrachloride to crystalline tin dioxide is a dynamic process, which proceeds through the formation of different intermediate species, such as aqua-, chlorido-tin complexes.[50-57] To identify these moieties, tin tetrachloride was dissolved in water or ethanol with addition of small amounts of acid or base. Despite adding base, the

solutions remained acidic with pH < 1. Then the mixtures were sealed in a specially designed glass ampule (Figure S1 in the SI) and studied by using solid-state ^{119}Sn NMR.
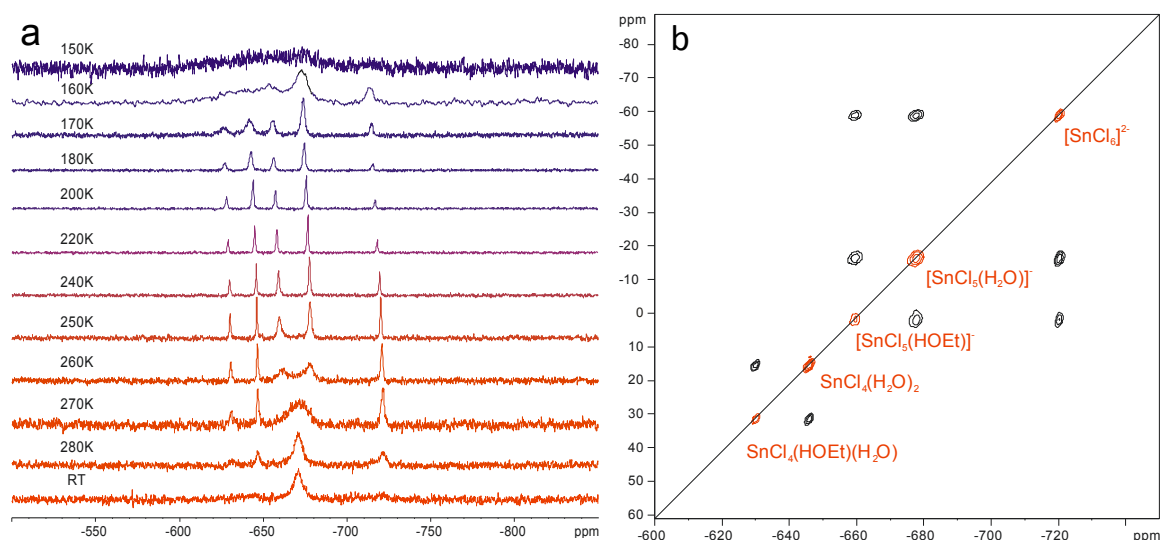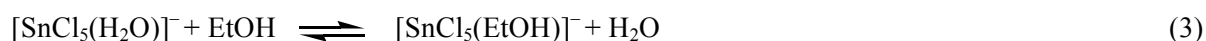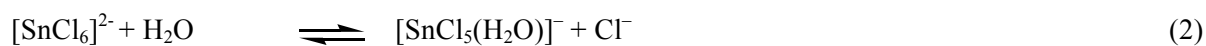

Figure 2. ^{119}Sn static NMR of SnCl$_4$ solution (SnCl$_4$:EtOH:HCl =1:22.98:10.25 molar ratio). (a) Low temperature ^{119}Sn static NMR spectra obtained upon cooling the sample from room temperature (RT) to 150K. (b) ^{119}Sn static 2D exchange NMR measured at 250 K, mixing time τ_m = 40 ms.

NMR patterns of a SnCl$_4$ solution in Figure 2a reveal a broad signal at about -670 ppm at room temperature. Upon cooling, the broad signal splits into five distinct sharp peaks. These signals observed in the range from -608 to -721 ppm are typical for octahedral tin (IV) complexes.[50] The six-fold coordination number instead of initial four-fold geometry can be explained by the fact that when tin tetrachloride is dissolved, the coordination number expands due to the bonding with chloride and an O-donor such as water and ethanol. Table 1 summarizes the tin-containing complexes detected in aqueous solutions containing ethanol, water with base or acid. The aqua- and chlorido- complexes were assigned according to previous studies (Table S2, in the SI).[50] The assignment of ethanolic complexes, however, was achieved by measuring ^3J (^{117}Sn-^{1}H)-couplings in ^{117}Sn low temperature MAS NMR (Figure S2 in the SI).

Table 1. Assignment of ^{119}Sn static NMR chemical shift values to the corresponding tin-containing complexes formed when tin tetrachloride is dissolved in ethanol and water.

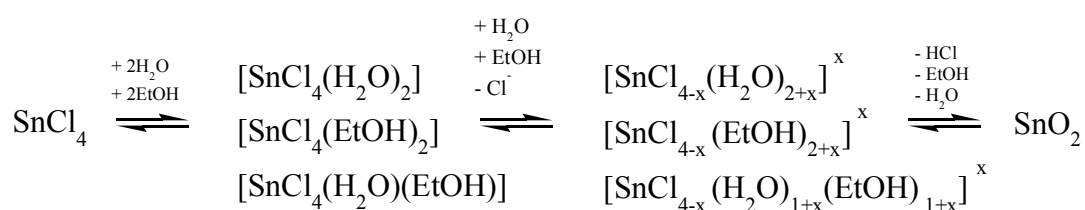| Species	$\delta(^{119}\text{Sn})$/ppm
$[\text{SnCl}_6]^{2-}$	-720
$[\text{SnCl}_5(\text{H}_2\text{O})]^-$	-677
$[\text{SnCl}_5(\text{EtOH})]^-$	-657
$[\text{SnCl}_4(\text{H}_2\text{O})_2]$	-647
$[\text{SnCl}_3(\text{H}_2\text{O})_3]^+$	-631
$[\text{SnCl}_4(\text{H}_2\text{O})(\text{EtOH})]$	-629

The tin complexes above exchange ligands with each other as the peaks lying on the main diagonal in the 2D NMR spectrum in Figure 2b have corresponding off-diagonal satellite peaks. These cross signals prove the exchange dynamics between the corresponding species and confirm the coalescence phenomena observed in room temperature measurements. Based on the ^{119}Sn static NMR data of the SnCl$_4$ solution shown in Figure 2, we propose that the tin-containing complexes undergo the following ligand exchange reactions:

$$[\text{SnCl}_6]^{2-} + \text{H}_2\text{O} \rightleftharpoons [\text{SnCl}_5(\text{H}_2\text{O})]^- + \text{Cl}^- \tag{2}$$

$$[\text{SnCl}_5(\text{H}_2\text{O})]^- + \text{EtOH} \rightleftharpoons [\text{SnCl}_5(\text{EtOH})]^- + \text{H}_2\text{O} \tag{3}$$

$$[\text{SnCl}_5(\text{EtOH})]^- + \text{Cl}^- \rightleftharpoons [\text{SnCl}_6]^{2-} + \text{EtOH} \tag{4}$$

$$[\text{SnCl}_4(\text{H}_2\text{O})_2] + \text{EtOH} \rightleftharpoons [\text{SnCl}_4(\text{EtOH})(\text{H}_2\text{O})] + \text{H}_2\text{O} \tag{5}$$

In the above sample, we did not detect any polymeric species with multiple metal atoms and oxygen bridging characteristic for condensation reactions. To increase the hydrolysis rate and to promote condensation, base was added to SnCl$_4$ solutions. In this case, additional signals in the less negative chemical shift region > -645 ppm appeared (Figure S3 in the SI). The signal shift towards higher chemical shifts indicates the formation of deeply hydrolyzed tin tetrachloride complexes, where more chloride ligands were exchanged by oxygen-containing ligands.[49] A broad signal at around -600 ppm observed for a base-containing tin tetrachloride solution (Figure S4 in the SI) can be attributed to the formation of OH-bridged structures.

However, the detailed characterization of this signal is challenging, due to a range of condensation products with similar spectral signature, the high sensitivity to aggregation and the precipitation of tin oxide.[58,59] In general, any signal in the range -629 to -608 ppm can be attributed to condensation products, such as oligomeric -Sn-O-Sn- structures.

To summarize, we have identified six tin chloride complexes that undergo dynamic ligand exchange when tin (IV) chloride is dissolved in ethanol and water (Table 1). We note that we did not consider isomerism of complexes, though the existence of cis/trans isomers has been previously discussed.[58] Our NMR study allows us to formulate Scheme 1, which reveals some of the intermediate moieties formed in the solution prior to condensation, polymerization and SnO_2 crystallization. The suggested mechanism is in line with the previous studies on tin oxide formation,[51-60] however it includes also the assignment of ethanolic complexes.

$$SnCl_4 \underset{+2EtOH}{\overset{+2H_2O}{\rightleftharpoons}} \begin{array}{l} [SnCl_4(H_2O)_2] \\ [SnCl_4(EtOH)_2] \\ [SnCl_4(H_2O)(EtOH)] \end{array} \underset{-Cl^-}{\overset{\substack{+H_2O \\ +EtOH}}{\rightleftharpoons}} \begin{array}{l} [SnCl_{4-x}(H_2O)_{2+x}]^x \\ [SnCl_{4-x}(EtOH)_{2+x}]^x \\ [SnCl_{4-x}(H_2O)_{1+x}(EtOH)_{1+x}]^x \end{array} \underset{\substack{-EtOH \\ -H_2O}}{\overset{-HCl}{\rightleftharpoons}} SnO_2$$

Scheme 1. Key elements of the mechanism of tin oxide formation via sol-gel processes when tin tetrachloride is dissolved in ethanol and water.

The results of the above NMR investigations suggest that when $SnCl_4$ is dissolved in aqueous CNC suspension, it reacts immediately with water forming different complexes and releasing HCl as a reaction byproduct. CNC suspensions are usually stable in aqueous media due to the negative $-OSO_3$-groups grafted on the crystal surfaces during hydrolysis.[45] However, their colloidal stability can be disturbed at high ionic strength conditions. It has been shown that CNCs aggregate when the ionic strength is above 25-40 mM.[61] The excessive acidity in tin tetrachloride aqueous solutions leads to an ionic strength higher than that threshold, causing poor colloidal stability of CNCs. Additionally, an increasing concentration of charged

moieties can change the overall ionic strength of the solution, and hence may negatively affect the colloidal stability of CNC. All the species in Table 1 have different charges; at early hydrolysis, negatively charged complexes dominate, whereas positively charged species are formed during prolonged hydrolysis and condensation.

To study the homogeneity of precursor solutions, we prepared different CNC and tin tetrachloride suspensions, containing small amounts of acid, base or ethanol. The as-prepared solutions were drop-cast on microscope slides and analyzed by using an optical microscope in dark field mode. Figure 3 shows that the solutions contain aggregates in the case of ethanol, concentrated acid or when the stirring time was too short (Figures 3a, b and c, respectively). However, a mixed colloid prepared without ethanol or acid and stirred overnight was homogeneous without visible macroscopic aggregates (Figure 3d). The only defects observed in this sample arise from cracks formed during the drying process (Figure S5 and S6 in the SI).
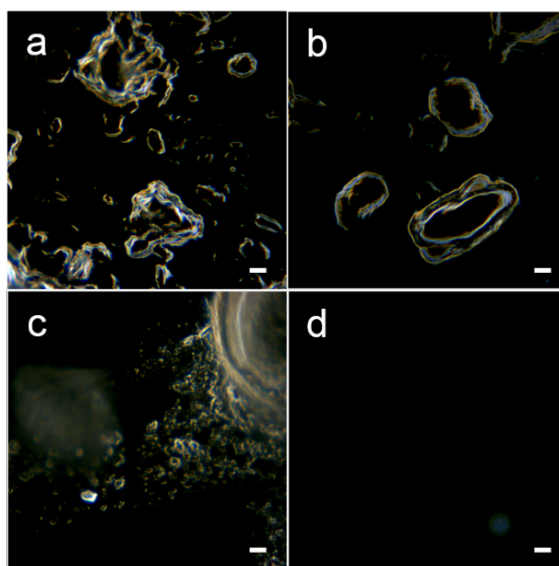

Figure 3. Dark field optical microscopy images of precursors cast on glass slides (from 2 wt% CNC suspensions in 0.2 M $SnCl_4$ in ethanol or water): (a) ethanolic suspension $SnCl_4$/EtOH/CNC, (b) aqueous suspension containing acid: $SnCl_4$/H_2O/CNC/1M HCl, (c) aqueous suspension $SnCl_4$/H_2O/CNC after 1 h stirring and (d) aqueous suspension $SnCl_4$/CNC/H_2O after overnight

stirring. The image (d) does not show any contrast, which indicates film homogeneity and absence of macroscopic aggregates. Scale bars: 0.2 mm.

These results suggest that despite the excess of H^+, which is known to decrease the colloidal stability of the CNCs, the aggregation of the suspension can be reversible to a certain extent and that large aggregates were removed by stirring overnight.

Prolonged stirring is beneficial for several reasons. First, large initial aggregates can mechanically disintegrate into smaller clusters. Second, during aging the precursor solution keeps changing on a molecular level. These changes also include the charge of the molecular precursors, their interactions with the negatively charged CNCs and the resulting change in electrostatic stabilization of the CNCs.

To prepare tin oxide films, we mixed colloidal CNCs with tin tetrachloride in water according to the optimized protocol that provides homogeneous aggregate-free nanocomposites. After stirring for at least 2 h, the solution was coated on substrates and then calcined at 400 °C to 600°C. Figures 4a-d show the SEM images of CNC-templated tin oxide films after calcination at 400 °C. The top-view image in Figure 4a reveals the film homogeneity and nanoscale porosity. Furthermore, the pore pattern resembles the features of pristine CNCs. Differently oriented anisotropic domains can be attributed to the self-assembly of the rod-like cellulose nanocrystals.[62] One such domain with pronounced anisotropic pore organization is shown in Figure 4c. Such domain formation was not observed for the films prepared from precursor solutions with lower or higher tin concentration compared to the latter sample (Figure 4b, d and Figures S7). Hence, the concentration of tin tetrachloride strongly affects the film morphology, in particular, the dimensions and the shape of pores and pore walls.

The average crystallite/domain size revealed by TEM and XRD for the CNC-templated tin dioxide is in the range from 9 to 20 nm, depending on calcination temperature, with larger

crystallite sizes characteristic for increasing calcination temperatures up to 600 °C (Figures S8, S9a and S11 in the SI). The specific surface area of CNC-templated films measured with nitrogen sorption experiments is in the range of 46 to 64 m^2/g, depending on precursor composition and calcination procedure (Figure S9b and Table S3 in the SI). The optimized protocol using 0.2 M SnCl$_4$ and 2 %wt. CNCs in water provided a crystal domain size of tin dioxide of about 9 nm and a specific surface area of 46 m^2/g. The pore diameters in these films range from 10 to 20 nm, with a maximum at 14 nm (Figure S9b in the SI).
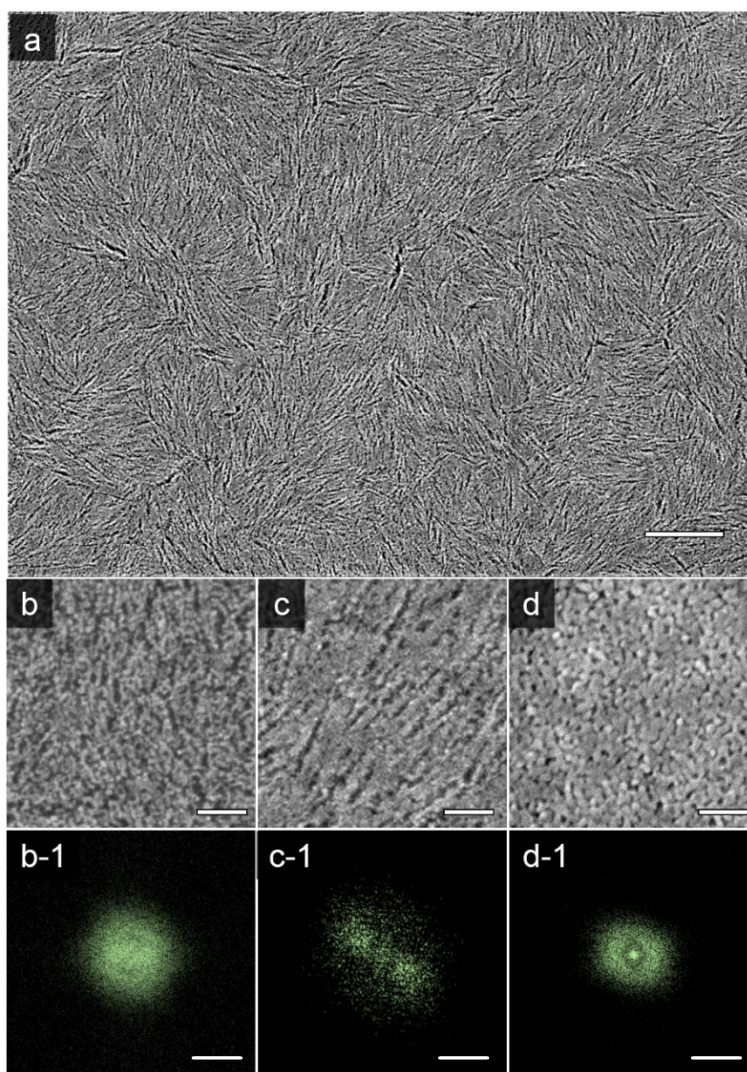

Figure 4. SEM top-view images of tin oxide thin films prepared from 0.2 M (a, c), 0.05 M (b) and 0.3 M (d) tin chloride in 2 wt% aqueous suspension of cellulose nanocrystals. The suspensions were coated on silicon wafers and calcined at 400 °C. (b-1, c-1, d-1) Fourier transformation (FFT) images

of (b), (c) and (d) patterns, respectively, obtained by using ImageJ software. Scale bars: 500 nm (a) and 100 nm (b – d).

Tin dioxide is an *n*-type semiconductor and one of the most important materials for the fabrication of resistive gas sensors. Its electronic conductivity is strongly affected by surface-chemical reactions with reducing or oxidizing gas molecules. Hence, measuring the ohmic resistance allows monitoring the presence of such gases at low ppm concentrations.[63]

For the device fabrication, we deposited CNC-templated SnO_2 on pre-fabricated sensor substrates that feature a platinum electrode structure for electrical contact and integrated heating for controlling the operating temperature. The colloidal mixture of tin tetrachloride and cellulose nanocrystals was deposited directly on the sensor substrates. Calcination, i.e. formation of SnO_2 and combustion of the CNC template was performed *in-situ* on the sensor at 400 °C (Figure 5d and Figure S10 in the SI).
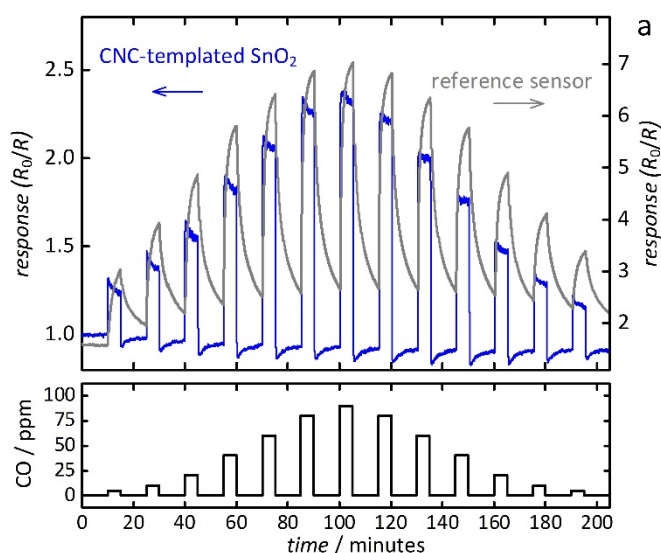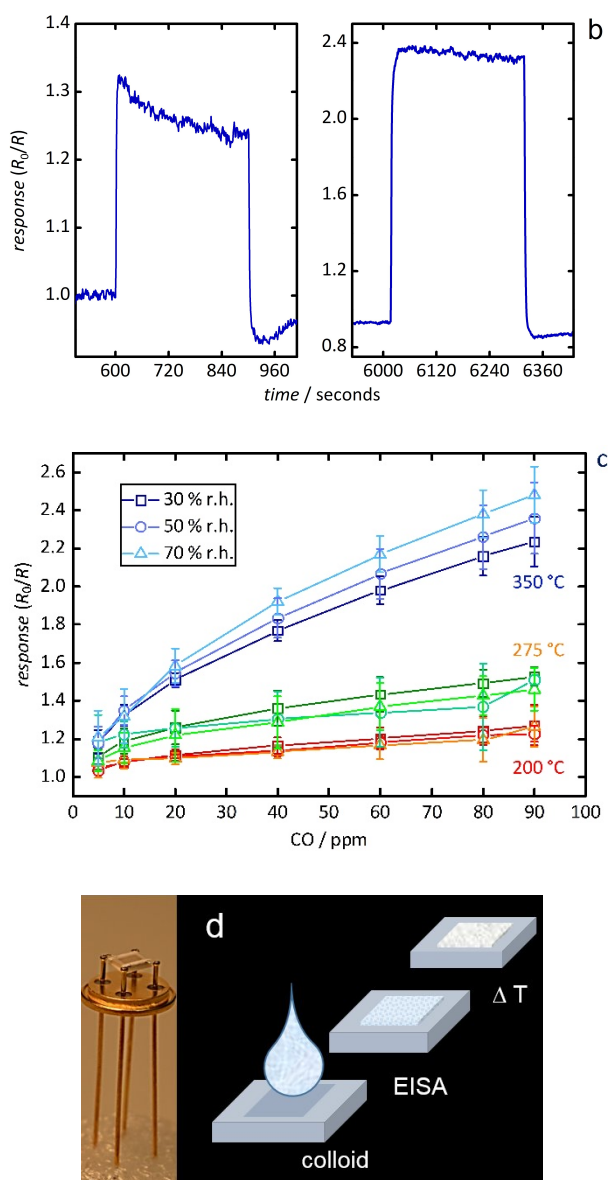
Figure 5. Performance of the CNC-templated tin dioxide CO sensor. (a) Sensor response to CO gas measured at 350 °C and 50 % relative humidity compared to a reference SnO_2-based commercial sensor UST GGS 1330; (b) blow-up of the two response peaks for 5 ppm (left) and 90 ppm (right); (c) CO concentration-dependent response values for variable different operating temperatures and relative humidity; (d) photograph of the sensor substrate (left) and schematic of the fabrication procedure of for the CNC-templated porous tin dioxide sensor (right). EISA: Evaporation-induced self-assembly.

Carbon monoxide (CO) was chosen as the analyte gas in concentrations between 5 ppm and 90 ppm. This is the relevant concentration range for hazard prevention; for example, the work-place threshold value for CO is 35 ppm in Germany.[64] The relative humidity was varied between 30 % and 70 % to assess the sensor's cross-sensitivity to water. The operating temperature was varied between 200 °C and 350 °C.

Figure 5a shows the CNC-templated SnO_2 sensor response to CO at 350 °C and 50 % relative humidity (r.h.). The 'response' is the change in ohmic resistance defined here as R_0/R, where R is the measured resistance and R_0 is the initial resistance before the analyte gas is offered (in synthetic air; 80 % N_2, 20 % O_2). During the measurements CO was dosed in pulses of 5 minutes each; the interval between pulses was 10 minutes. The response of a commercially available reference sensor was measured simultaneously for comparison (see Experimental section). The reference sensor works based on the same resistive principle, i.e. its response is based on a change in the ohmic resistance upon interaction with the CO analyte molecules. Both sensors show an approximately linear response to the CO concentration. Moreover, the response of the CNC templated tin oxide sensor in terms of relative resistance is weaker than that of the reference sensor, it is however substantially faster. Figure 5b shows a blow-up of two response peaks (5 ppm and 90 ppm, respectively), demonstrating the remarkably fast response. The t_{90} value (time until 90 % of maximum signal) is only 3 seconds and the signal decay after the CO pulse is similarly fast. These findings may be explained by the small thickness (<0.5 μm) of the porous SnO_2 layer, enabling fast diffusion of gas molecules, and by the large surface-to-volume ratio (A_{BET} = 46 m^2 g^{-1}, Figure S9 in the SI). The t_{90} value of the reference sensor is much higher; it cannot be assessed quantitatively, since signal saturation is not reached within the 5 minutes of the CO pulses, *i.e.* the maximum signal strength is unknown. Other mesoporous SnO_2-based sensors reported in the literature exhibit

t_{90} values in their CO response between 10 seconds and several minutes under similar conditions.[65-67]

Figure 5c shows the response values for CO measurements at relative humidities of 30 %, 50 %, and 70 %, each at operating temperatures of 200 °C, 275 °C, and 350 °C. The humidity has only little impact on the response at low operating temperature; a slightly higher humidity dependence is observed at high temperature. All in all, the sensor turns out to be fairly robust against changes in humidity. It is also obvious from Figure 5c that the strongest response is obtained at 350 °C, while only little difference is observed between 200 °C and 275 °C. Such temperature-dependent behavior is frequently observed for resistive gas sensors.[68]

Additionally, the *in-situ* preparation of the porous film yields a sensor device with a mechanically stable connection between active layer and substrate and a strong electrical contact to the electrodes. The resulting SnO_2 porous layer exhibits nano-crystallinity (average grain size: 9 nm), which is favorable for high sensor performance.[69,70]

5. Conclusions

In summary, we successfully developed a scalable, straightforward and economically valuable, highly reproducible method to fabricate porous CNC-templated SnO_2 films with high crystallinity. By investigating the molecular composition of precursor solutions we optimized the colloidal stability of CNCs in the presence of tin tetrachloride. As a result, we report an optimized precursor preparation protocol that provides homogeneous porous thin films with nanoscale morphological features, high porosity and pore sizes of around 10 nm. This method was then successfully exploited to produce CO gas sensors with fast response in the ppm range and low cross-sensitivity to humidity.

6. Associated content

Supporting Information

A table with recipes for the $SnCl_4$ solutions studied by using NMR analysis; a schematic of a glass sample container for the ^{119}Sn static NMR measurements; a table with NMR chemical shift values characteristic for different tin compounds; NMR spectra and chemical shift values detected for different tin tetrachloride solutions; a photograph of CNC and tin tetrachloride solutins; optical images of CNC-tin tetrachloride nanocomposites; electron microscopy, XRD and nitrogen sorption measurements of CNC-templated tin dioxide.

This material is available free of charge via the Internet at http://pubs.acs.org.

References

1.   Brezesinski, T.; Fischer, A.; Iimura, K.-i.; Sanchez, C.; Grosso, D.; Antonietti, M.; Smarsly, B. Generation of Self Assembled 3D Mesostructured SnO_2 Thin Films with Highly Crystalline Frameworks. *Adv. Funct. Mater.* **2006**, *16*, 1433-1440.

2.   Li, F.; Lu, C; Knowles, G. P.; MacFarlane D. R.; Zhang, J. Hierarchical Mesoporous SnO_2 Nanosheets on Carbon Cloth: A Robust and Flexible Electrocatalyst for CO_2 Reduction with High Efficiency and Selectivity. *Angew. Chem.* **2017**, 129, 520-524.

3. Park, G. D.; Lee, J. K., Kang, Y. C. Synthesis of Uniquely Structured SnO_2 Hollow Nanoplates and Their Electrochemical Properties for Li Ion Storage *Adv. Funct. Mater.* **2017**, 27, 1603399.

4. Fried, D. I.; Ivanova, A.; Muller, V.; Rathousky, J.; Smarsly, B. M.; Fattakhova-Rohlfing, D. A Facile Synthesis of Mesoporous Crystalline Tin Oxide Films Involving a Base-Triggered Formation of Sol-Gel Building Blocks. *Nanoscale* **2011**, *3*, 1234-1239.

5. Martinez, C. J.; Hockey, B.; Montgomery, C. B.; Semancik, S. Porous Tin Oxide Nanostructured Microspheres for Sensor Applications. *Langmuir* **2005**, *21*, 7937-7944.

6. Zhou, M.; Liu, Y.; Chen, J.; Yang, X. Double Shelled Hollow SnO_2/Polymer Microsphere as a High-Capacity Anode Material for Superior Reversible Lithium Ion Storage. *J. Mater. Chem. A* **2015,** *3*, 1068-1076.

7. Li, N.; Song, L.; Bießmann, L.; Xia, S.; Ohm, W.; Brett, C. J.; Hadjixenophontos, E.; Schmitz, G.; Roth: S. V.; Müller Buschbaum, P.; Morphology Phase Diagram of Slot Die Printed TiO2 Films Based on Sol–Gel Synthesis. *Adv. Mater. Interfaces* **2019**, *6*, 2196-7350.

8. Grosso, D.; Cagnol, F.; Soler-Illia, G. J. d. A. A.; Crepaldi, E. L.; Amenitsch, H.; Brunet-Bruneau, A.; Bourgeois, A.; Sanchez, C. *Adv. Funct. Mater.* **2004**, *14*, 309 - 322.

9. Sun, Y.-F.; Liu, S.-B.; Meng, F.-L.; Liu, J.-Y.; Jin, Z.; Kong, L.-T.; Liu, J.-H. Metal Oxide Nanostructures and Their Gas Sensing Properties: A Review. *Sensors* **2012**, *12*, 2610.

10. Long, H.; Harley-Trochimczyk, A.; He, T.; Pham, T.; Tang, Z.; Shi, T.; Zettl, A.; Mickelson, W.; Carraro, C.; Maboudian, R. In Situ Localized Growth of Porous Tin

Oxide Films on Low Power Microheater Platform for Low Temperature CO Detection. *ACS Sensors* **2016**, *1*, 339-343.

11. Zhao, X.; Shi, W.; Mu, H.; Xie, H.; Liu, F. Templated Bicontinuous Tin Oxide Thin Film Fabrication and the NO_2 Gas Sensing. *J. Alloys Comp.* **2016**, *659*, 60-65.

12. Li, F.; Chen, L.; Knowles, G. P.; MacFarlane, D. R.; Zhang, J. Hierarchical Mesoporous SnO_2 Nanosheets on Carbon Cloth: A Robust and Flexible Electrocatalyst for CO_2 Reduction with High Efficiency and Selectivity. *Angew. Chem.* **2017**, *56*, 505-509.

13. Aoki, Y.; Huang, J.; Kunitake, T. Electro-Conductive Nanotubular Sheet of Indium Tin Oxide as Fabricated from the Cellulose Template. *J. Mater. Chem.* **2006,** *16*, 292-297.

14. Guo, H.; Mao, R.; Yang, X.; Wang, S.; Chen, J. Hollow Nanotubular SnO_2 with Improved Lithium Storage. *J. Power Sources* **2012**, *219*, 280-284.

15. Wang, K.; Wang, M.; Huang, J. Natural Cellulose Derived Tin Nanoparticle/Carbon Nanofiber Composite as Anodic Material in Lithium Ion Batteries. *ChemNanoMat* **2016**, *2*, 1040-1046.

16. Huang, J.; Matsunaga, N.; Shimanoe, K.; Yamazoe, N.; Kunitake, T. Nanotubular SnO_2 Templated by Cellulose Fibers: Synthesis and Gas Sensing. *Chem. Mater.* **2005**, *17*, 3513-3518.

17. Gu, Q.; Nagai, K.; Nakai, M.; Norimatsu, T. Polymorphic Tin Dioxide Synthesis via Sol-Gel Mineralization of Ethyl-Cyanoethyl Cellulose Lyotropic Liquid Crystals. *Colloid Polym. Sci.* **2006,** *284*, 429-434.

18. Nagai, K.; Gu, Q.; Yasuda, Y.; Norimatsu, T.; Fujioka, S.; Nishimura, H.; Miyanaga, N.; Izawa, Y.; Mima, K. Oriented and Low Density Tin Dioxide Film by Sol-Gel Mineralizing Tin Contained Hydroxypropyl Cellulose Lyotropic Liquid Crystal for Laser Induced Extreme Ultraviolet Emission. *J. Polym. Sci. A* **2009**, *47*, 4566-4576.

19. Mahadeva, K. S.; Kim, J. Hybrid Nanocomposite Based on Cellulose and Tin Oxide: Growth, Structure, Tensile and Electrical Characteristics. *Sci. Technol. Adv. Mater.* **2011**, *12*, 055006.

20. Song, F.; Su, H.; Chen, J.; Moon, W.-J.; Lau, W. M.; Zhang, D. 3D Hierarchical Porous SnO_2 Derived from Self-Assembled Biological Systems for Superior Gas Sensing Application *J. Mater. Chem.* **2012,** *22*, 1121-1126.

21. Zhang, C.; Wang, J.; Hu, R.; Qiao, Q.; Li, X. Synthesis and Gas Sensing Properties of Porous Hierarchical SnO_2 by Grapefruit Exocarp Biotemplate. *Sens. Actuators B* **2016**, *222*, 1134-1143.

22. Manjula, P.; Boppella, R.; Manorama, S. V. A Facile and Green Approach for the Controlled Synthesis of Porous SnO_2 Nanospheres: Application as an Efficient Photocatalyst and an Excellent Gas Sensing Material. *ACS Appl. Mater. Interf.* **2012**, *4*, 6252-6260.

23. Lu, Y.; Poole Ii, J. E.; Aytug, T.; Meyer Iii, H. M.; Ozcan, S. Tunable Morphologies of Indium Tin Oxide Nanostructures Using Nanocellulose Templates. *RSC Advances* **2015**, *5*, 103680-103685.

24. Foster, E. J.; Moon, R. J.; Agarwal, U. P.; Bortner, M. J.; Bras, J.; Camarero-Espinosa, S; Chan, Kathleen J.; Clift, M. J. D.; Cranston, E. D.; Eichhorn, S. J.; Fox, D. M.; Hamad, W. Y.; Heux, L.; Jean, B.; Korey, M.; Nieh, W.; Ong, K. J.; Reid, M. S.; Renneckar, S.; Roberts, R.; Shatkin, J. A.; Simonsen, J.; Stinson-Bagby, Kelly.; Wanasekara, N.; Youngblood, J. Current Characterization Methods for Cellulose Nanomaterials. *Chem. Soc. Rev.* **2018**, 47, 2609-2679.

25. Kontturi, E.; Laaksonen, P.; Linder, M. B.; Nonappa; Gröschel A. H.; Rojas, O. J.; Ikkala O. Advanced Materials through Assembly of Nanocelluloses. *Adv. Mater.* **2018**, *30*, 1703779.

26. Frka-Petesic, B.; Guidetti, G.; Kamita, G.; Vignolini S. Controlling the Photonic Properties of Cholesteric Cellulose Nanocrystal Films with Magnets. *Adv. Mater.* **2017**, 29, 1701469.

27. Parker, R. M.; Guidetti G.; Williams, C. A.; Zhao, T.; Narkevicius, A.; Vignolini, S.; Frka-Petesic, B. The Self Assembly of Cellulose Nanocrystals: Hierarchical Design of Visual Appearance. *Adv. Mater*. **2018**, *30*, 1704477.

28. Shi, Z,; Phillips, G. O.; Yang, G. Nanocellulose Electroconductive Composites. *Nanoscale* **2013**, *5*, 3194-3201.

29. Meseck, G. R.; Terpstra, A. S.; MacLachlan, M. J. Liquid crystal templating of nanomaterials with nature's toolbox. *Curr. Opin. Colloid Interface Sci.* **2017**, *29*, 9-20.

30. Giese, M.; Blusch, L. K.; Khan, M. K.; MacLachlan, M. J. Functional Materials from Cellulose Derived Liquid Crystal Templates. *Angew. Chem. Int. Ed.* **2015**, *54*, 2888-2910.

31. Tian, H.; He, J. Cellulose as a Scaffold for Self-Assembly: From Basic Research to Real Applications. *Langmuir* **2016**, *32*, 12269-12282.

32. Sun, M.-H.; Huang, S.-Z.; Chen, L.-H.; Li, Y.; Yang, X.-Y.; Yuan, Z.-Y.; Su, B.-L. Applications of Hierarchically Structured Porous Materials from Energy Storage and Conversion, Catalysis, Photocatalysis, Adsorption, Separation, and Sensing to Biomedicine. *Chem. Soc. Rev.* **2016**, *45*, 3479-3563.

33. Tingaut, P.; Zimmermann, T.; Sebe, G. Cellulose Nanocrystals and Microfibrillated Cellulose as Building Blocks for the Design of Hierarchical Functional Materials. *J. Mater. Chem.* **2012**, *22*, 20105-20111.

34. Lukach, A.; Thérien-Aubin, H.; Querejeta-Fernández, A.; Pitch, N.; Chauve, G.; Méthot, M.; Bouchard, J.; Kumacheva, E. Coassembly of Gold Nanoparticles and Cellulose Nanocrystals in Composite Films. *Langmuir* **2015**, *31*, 5033-5041.

35. Ivanova, A.; Fravventura, M. C.; Fattakhova-Rohlfing, D.; Rathouský, J.; Movsesyan, L.; Ganter, P.; Savenije, T. J.; Bein, T. Nanocellulose-Templated Porous Titania Scaffolds Incorporating Presynthesized Titania Nanocrystals. *Chem. Mater.* **2015**, *27*, 6205-6212.

36. Shopsowitz, K. E.; Qi, H.; Hamad, W. Y.; MacLachlan, M. J. Free-Standing Mesoporous Silica Films with Tunable Chiral Nematic Structures. *Nature* **2010**, *468*, 422-425.

37. Kelly, J. A.; Giese, M.; Shopsowitz, K. E.; Hamad, W. Y.; MacLachlan, M. J. The Development of Chiral Nematic Mesoporous Materials. *Acc. Chem. Res.* **2014**, *47*, 1088-1096.

38. Brinker, J. C.; Scherer, G. W. *Sol-Gel Science: The Physics and Chemistry of Sol-Gel*. Academic Press: London, 1990.

39. Sheikhi, A.; Kakkar, A.; van de Ven, T. G. M. A Leaf out of Nature's Book: Hairy Nanocelluloses for Bioinspired Mineralization. *Crystal Growth & Design* **2016**, *16*, 4627-4634.

40. Sachse, A.; Cardoso, L.; Kostov, K. L.; Gérardin, C.; Belamie, E.; Alonso, B. Mesoporous Alumina from Colloidal Biotemplating of Al Clusters. *Chem.: Eur. J.* **2015**, *21*, 3206-3210.

41. Livage, J. Sol-Gel Synthesis of Heterogeneous Catalysts from Aqueous Solutions. *Catal. Today* **1998**, *41*, 3-19.

42. Zhong, L.; Fu, S.; Peng, X.; Zhan, H.; Sun, R. Colloidal Stability of Negatively Charged Cellulose Nanocrystalline in Aqueous Systems. *Carbohydr. Polym.* **2012**, *90*, 644-649.

43. Revol, J.-F.; Godbout, L.; Gray, D. G. *Solid Self-Assembled Films of Cellulose with Chiral Nematic Order and Optically Variable Properties*. Pulp and Paper Technical Association of Canada: Montreal, PQ, Canada, 1998; Vol. 24.

44. Parker, R. M.; Frka-Petesic, B.; Guidetti, G.; Kamita, G.; Consani, G.; Abell, C.; Vignolini, S. Hierarchical Self-Assembly of Cellulose Nanocrystals in a Confined Geometry. *ACS Nano* **2016**, *10*, 8443-8449.

45. Beck, S.; Méthot, M.; Bouchard, J. General Procedure for Determining Cellulose Nanocrystal Sulfate Half-Ester Content by Conductometric Titration. *Cellulose* **2015**, *22*, 101-116.

46. Harris, R. K.; Becker, E. D; Cabral de Meneze, S. M; Granger, P.; Hoffman, R. E; Zilm, K.W. Further Conventions for NMR Shielding and Chemical Shifts (IUPAC Recommendations 2008). *Pure Appl.Chem.* **2008**, *80*, 59-84.

47. Scherrer, P. *Bestimmung der Größe und der inneren Struktur von Kolloidteilchen mittels Röntgenstrahlen*. In: *Nachrichten von der Gesellschaft der Wissenschaften zu Göttingen, Mathematisch-Physikalische Klasse*. Weidmannsche Buchhandlung, Berlin **1918**, 98-100.

48. Brunauer, S.; Emmett P. H, Teller, E. Adsorption of Gases in Multimolecular Layers, *Am. Chem. Soc.* **1938**, *60*, 309-319.

49. www.umweltsensortechnik.de

50. Taylor, M. J.; Coddington, J. M. The Constitution of Aqueous Tin(IV) Chloride and Bromide Solutions and Solvent Extracts Studied by ^{119}Sn NMR and Vibrational Spectroscopy. *Polyhedron* **1992**, *11*, 1531-1544.

51. Burke, J. J.; Lauterbur, P. C. Sn[119] Nuclear Magnetic Resonance Spectra. *J. Am. Chem. Soc.* **1961**, *83*, 326-331.

52. Colton, R.; Dakternieks, D.; Harvey, C.-A. Phosphorus-31 and Tin-119 NMR Studies on Tin(IV) Halides and Their Adducts. *Inorg. Chim. Acta* **1982**, *61*, 1-7.

53. Hani, R.; Geanangel, R. A. ^{119}Sn NMR in Coordination Chemistry. *Coord. Chem. Rev.* **1982**, *44*, 229-246.

54. Mitchell, T. N. On the Relation between Element NMR Chemical Shifts in the Fourth Main Group. *J. Organomet. Chem.* **1983**, *255*, 279-285.

55. Dillon, K. B.; Marshall, A. Tin-119 Nuclear Magnetic Resonance Studies of some Pseudohalogeno-Derivatives of $[SnX_6]^{2-}$(X = Cl or Br). *J. Chem. Soc. Dalton Trans.* **1987**, 315-317.

56. Clayden, N. J.; Dobson, C. M.; Fern, A. High-Resolution Solid-State Tin-119 Nuclear Magnetic Resonance Spectroscopy of Ternary Tin Oxides. *J. Chem. Soc. Dalton Trans.* **1989**, 843-847.

57. Mao, X.-A.; You, X.-Z.; Dai, A.-B. Study of Hydrolytic Kinetics of the Hexachlorostannate Anion by Two   Dimensional [119]Sn Exchange Spectroscopy. *Magn. Reson. Chem.* **1989**, *27*, 836-840.

58. Jensen, K. M. Ø.; Christensen, M.; Juhas, P.; Tyrsted, C.; Bøjesen, E. D.; Lock, N.; Billinge, S. J. L.; Iversen, B. B. Revealing the Mechanisms behind SnO_2 Nanoparticle Formation and Growth during Hydrothermal Synthesis: An In Situ Total Scattering Study. *J. Am. Chem. Soc.* **2012**, *134*, 6785-6792.

59. Caetano, B. L.; Meneau, F.; Santilli, C. V.; Pulcinelli, S. H.; Magnani, M.; Briois, V. Mechanisms of SnO_2 Nanoparticles Formation and Growth in Acid Ethanol Solution Derived from SAXS and Combined Raman-XAS Time-Resolved Studies. *Chem. Mater.* **2014**, *26*, 6777-6785.

60.   Ruzicka, S.; Merbach, A. Adducts of Tin(IV) Tetrahalides with Neutral Lewis Bases. II. Quantitative Study of the Cis-Trans Equilibria by NMR. *Inorg. Chim. Acta* **1977**, *22*, 191-200.

61.   Phan-Xuan, T., Thuresson, A., Skepö, M.; Labrador, A.; Bordes, R.; Matic, A. Aggregation Behavior of Aqueous Cellulose Nanocrystals: the Effect of Inorganic Salts. *Cellulose* **2016**, *23*, 3653-3664.

62.   Brett, C. J.; Mittal, N.; Ohm, W.; Gensch, M.; Kreuzer, L. P.; Körstgens, V.; Månsson, M.; Frielinghaus, H.; Müller-Buschbaum, P.; Söderberg, L. D.; Roth, S. V. Water-Induced Structural Rearrangements on the Nanoscale in Ultrathin Nanocellulose Films. *Macromolecules* **2019**, *52*, 12, 4721-4728.

63.   Tiemann, M. Porous Metal Oxides as Gas Sensors. *Chem.: Eur. J.* **2007**, *13*, 8376-8388.

64.   *Technische Regeln für Gefahrstoffe* (TRGS 900), BArBl 1/2006, p. 41-55.

65.   Wagner, T.; Kohl, C.-D.; Fröba, M.; Tiemann, M. Gas Sensing Properties of Ordered Mesoporous SnO_2. *Sensors* **2006**, *6*, 318-323.

66.   De, G.; Köhn, R.; Xomeritakis, G.; Brinker, C. J. Nanocrystalline Mesoporous Palladium Activated Tin Oxide Thin Films as Room-Temperature Hydrogen Gas Sensors. *Chem. Commun.* **2007**, 1840-1842.

67.   Waitz, T.; Becker, B.; Wagner, T.; Sauerwald, T.; Kohl, C.-D.; Tiemann, M. Ordered Nanoporous SnO_2 Gas Sensors with High Thermal Stability. *Sens. Actuators B* **2010**, *150*, 788-793.

68.   Wagner, T.; Haffer, S.; Weinberger, C.; Klaus, D.; Tiemann, M. Mesoporous Materials as Gas Sensors. *Chem. Soc. Rev.* **2013**, *42*, 4036-4053.

69.   Xu, C.; Tamaki, J.; Miura, N.; Yamazoe, N. Grain Size Effects on Gas Sensitivity of Porous SnO_2-Based Elements. *Sens. Actuators B* **1991**, *3*, 147-155.

70. Kozhushner, M. A.; Trakhtenberg, L. I.; Bodneva, V. L.; Belisheva, T. V.; Landerville, A. C.; Oleynik, I. I. Effect of Temperature and Nanoparticle Size on Sensor Properties of Nanostructured Tin Dioxide Films. *J. Phys. Chem. C* **2014,** *118*, 11440-11444.

TOC graphic: